

Membrane MOT: Trapping Dense Cold Atoms in a Sub-Millimeter Diameter Hole of a Microfabricated Membrane Device

Jongmin Lee (✉ jongmin.lee@sandia.gov)

Sandia National Laboratories

Grant Biedermann

University of Oklahoma

John Mudrick

Sandia National Laboratories

Erica Douglas

Sandia National Laboratories

Yuan-Yu Jau

Sandia National Laboratories

Research Article

Keywords: Membrane MOT, Cold Atoms, Sub-Millimeter Diameter Hole, Microfabricate, Trapping Dense

Posted Date: November 24th, 2020

DOI: <https://doi.org/10.21203/rs.3.rs-107899/v1>

License:  This work is licensed under a Creative Commons Attribution 4.0 International License.

[Read Full License](#)

Version of Record: A version of this preprint was published at Scientific Reports on April 22nd, 2021. See the published version at <https://doi.org/10.1038/s41598-021-87927-z>.

Membrane MOT: Trapping Dense Cold Atoms in a Sub-Millimeter Diameter Hole of a Microfabricated Membrane Device

Jongmin Lee^{1,*}, Grant Biedermann², John Mudrick¹, Erica A. Douglas¹, and Yuan-Yu Jau¹

¹Sandia National Laboratories, Albuquerque, New Mexico 87185, USA

²Department of Physics and Astronomy, University of Oklahoma, Norman, Oklahoma 73019, USA

*jongmin.lee@sandia.gov

ABSTRACT

We present a demonstration of keeping a cold-atom ensemble within a sub-millimeter diameter hole in a transparent membrane. Based on the effective beam diameter of the magneto-optical trap (MOT) given by the hole diameter ($d = 400 \mu\text{m}$), we measure an atom number that is 10^5 times higher than the predicted value using the conventional d^6 scaling rule. Atoms trapped by the membrane MOT are cooled down to $10 \mu\text{K}$ with sub-Doppler cooling. Such a device can be potentially coupled to the photonic/electronic integrated circuits that can be fabricated in the membrane device representing a step toward the atom trap integrated platform.

Introduction

The past two decades have witnessed remarkable advances in computing and sensing demonstrations that leverage coherence and entanglement in systems well-described by quantum mechanics^{1,2}. Concurrently, the advent of microfabrication techniques promises to buttress the exploration of new frontiers in quantum applications³⁻⁵ through atom-light interactions⁶⁻¹⁶ in addition to incorporating compact MOTs¹⁷⁻²⁵ on atom chips²⁶⁻³³ and superconducting circuits³⁴⁻³⁸. Already, quantum engineering for integrated quantum systems has seen the development of compact and scalable laser systems using hybrid integrated photonic circuits^{39,40} with silicon photonics, III-V photonics and nonlinear optics. Such techniques are poised to expand reliable operation of cold-atom positioning, navigation and timing (PNT) sensors⁴¹ in new and challenging environments. Engineering of quantum systems has also enabled integrated, on-chip quantum computing platforms capable of individual spin addressing, spin-spin entanglement and spin readout. Quantum processors with more than 50 qubits have been demonstrated with superconducting circuits possible in the near future^{42,43}. Likewise, new efforts are exploring novel surface ion-trap platforms⁴⁴ combining microfabricated surface electrodes and integrated photonics on the same chip. These quantum engineering efforts seek to inaugurate a quantum-to-classical interface⁴⁵ to realize a true quantum device.

We demonstrate membrane MOT devices compatible with PIC technology⁴⁶, which can pave the way toward atom trap integrated platforms (ATIP) for neutral atoms. In this architecture, the suspended membrane waveguide can be used to trap and probe neutral atoms through the evanescent field of optical waveguide modes, and the heat generated at the waveguide can be dissipated through the membrane attached to the substrate, which can deliver sufficient guided optical powers in vacuum for evanescent-field optical traps. Thanks to the heat dissipation capability, there may be no need for the fabrication of optical waveguides on the substrate¹⁰⁻¹². Photonic ATIPs will be crucial for enabling future neutral atom quantum applications. Atomic spins positioned near the waveguide surface offer an interface between spin information and the guided optical mode which can be processed in the PIC. Compared to artificial counterparts^{47,48}, neutral atoms offer powerful and compelling advantages in terms of homogeneous physical properties and long coherence and life times due to being well-isolated from noisy materials. Compared to trapped ion approaches, neutral atoms offer near-term scaling advantages, larger atomic ensembles and wide-ranging sensing modalities.

In this paper, we demonstrate a foundational technique for laser cooling atoms directly in the vicinity of an optical information bus. This approach is advantageous in terms of technical simplicity and efficacy. In particular, efficient atom loading nearby the nanostructure is crucial for positioning and coupling many atoms, not a single atom, to the evanescent field of the guided mode. In so doing, we can connect the success efficient two-color evanescent-field atom trapping with nanofibers⁴⁹⁻⁵² to the unique features and possibilities of the photonic ATIP. Underpinning our approach is our introduction of a MOT produced in a sub-millimeter diameter hole on a microfabricated transparent membrane. The membrane itself can

support an optical waveguide that traverses the hole allows the optical field to interact with the atomic spins via the evanescent tail extending into the vacuum. In our demonstration, we imitate such a waveguide with a three-micron-width beam fabricated from the membrane material, allowing us to test the atom loading dynamics around such a structure.

It is well known that the number of atoms accumulated in a MOT scales unfavorably with MOT beam diameter (d), especially below 2 mm where the scaling converts from $1/d^{3.6}$ to $1/d^6$ ⁵³. In our system⁵⁴, we reimagine the interface between a MOT and a membrane MOT device with a transparent membrane that divides the MOT loading volume in two and provides a small membrane hole for cold atoms to collect. This is enabled by the overdamped harmonic motion of an atom that enters the loading volume. Through the laser cooling dynamics, atoms can quite often dissipate kinetic energy and relax into the center of the trap without entering the other hemisphere. Thus, many atoms eventually accumulate at the center of the membrane hole. This requires the diameter of the membrane hole to be larger than the diameter of the MOT cloud which can readily sub-mm, whereas the size of the membrane itself can be orders of magnitude larger and define a generous loading volume. The efficacy of this approach can be clearly shown by comparison with the achievable atom number in a MOT specified by cooling beam diameters limited by the diameter of the membrane hole. A MOT beam diameter limited by the 400 μm -hole diameter would yield a number of trapped atoms 10^5 times smaller than what we observe. Using the membrane MOT with the 400 μm -hole diameter, we achieved about 10^5 atoms, but the extrapolated atom number (d^6 scaling) from the open space MOT is less than

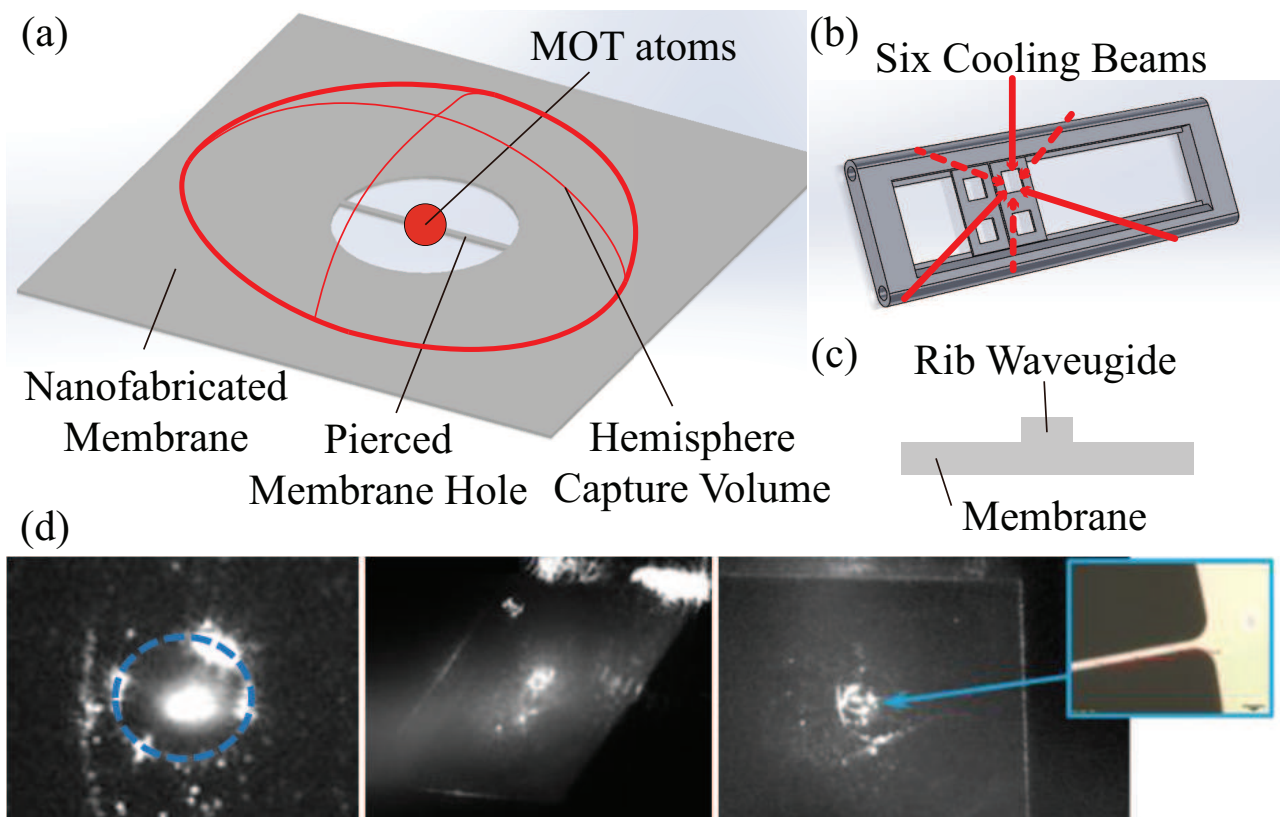


Figure 1. (a) Concept of membrane MOT devices. The area of the membrane is $5 \text{ mm} \times 5 \text{ mm}$, and cold atoms in a membrane MOT can be generated at a sub-millimeter diameter membrane hole using six 3.8 mm-diameter cooling beams. The pierced membrane hole imitates a $3\text{-}\mu\text{m}$ -width membrane rib waveguide, i.e., a dummy waveguide. (b) Six cooling beam configuration. Two membrane MOT devices are fabricated on the silicon substrate ($1 \text{ cm} \times 2 \text{ cm}$), which are attached on the aluminum mount with UV epoxy. (c) Concept of the membrane rib waveguide. (d) (Left) Image of laser-cooled atoms at the center of a membrane hole without a dummy waveguide. The diameter of the membrane hole is $400 \mu\text{m}$. (Middle, Right) Images of laser-cooled atoms at a pierced membrane hole. The diameter of the pierced membrane hole is $400 \mu\text{m}$.

one with the $400\ \mu\text{m}$ beam diameter. Furthermore, this geometry is compatible with sub-Doppler cooling mechanisms^{55–58} and allows temperature so $10\ \mu\text{K}$ to be reached in our setup. Our membrane MOT approach offers a convenient means for positioning a large number of trapped atoms within $300\ \mu\text{m}$ of a microfabricated structure in the plane of an ATIP.

Experimental setup and membrane fabrication

In the experiment, the ^{133}Cs atoms were used for the open space and membrane MOTs with the cooling and repump beams (852 nm, D2 transition) and the absorption probe (895 nm, D1 transition). The vacuum setup is configured with a glass chamber (40 mm×40 mm×100 mm), a mini-cube (Kimball Physics) and a 5 l/s ion pump. All the chamber platform can be moved with a 1D lab-jack and a 2D translation stage and be aligned to the MOT under the vacuum of 10^{-8} mbar. Six intensity balanced MOT beams are collimated with fiber-port collimators, and the small MOT beams ($< 4\ \text{mm}$ diameter) pass through the transparent membrane (5 mm × 5mm) and can be precisely aligned to the membrane hole, i.e., the MOT loading zone, using multiple 2D translation stages. Four horizontal laser cooling beams cool atoms in the horizontal plane, and two vertical laser cooling beams cool atoms along the vertical axis, i.e., the gravity direction. The transparent membrane captures atoms with two large hemispherical capture volumes as shown in Fig. 1 (a) and loads MOT atoms into the sub-millimeter membrane hole. An adapter with a groove-grabber between a mini-flanged cube and 2-3/4" CF flanged glass chamber firmly hold two stainless steel rods into the glass cell. The two rods support the aluminum membrane sample holder with ~ 40 degree angle, which allows the MOT beams can capture atoms without blocking MOT beams as shown in Fig. 1 (b). The axis of quadruple MOT coils is aligned to the vertical axis, i.e., the gravity direction. The MOT and X, Y, Z bias coils are prepared with 3D printed ULTEM mount, which can be aligned with the 2D translation stage. We checked Doppler-cooling and sub-Doppler cooling of free-space MOT and membrane MOT with/without a dummy waveguide at the center hole.

We have used two membranes made of AlN (Aluminum nitride) and SiN (Silicon nitride) for the experiments. Especially, the thermal conductivity of AlN is 10 times higher than SiN, which can be advantageous in terms of heat dissipation in vacuum. The absorption loss of membrane rib waveguides (Fig. 1 (c)) needs to be considered because it is the main cause of heat generation at the suspended waveguide section. The fabrication process of the membrane MOT devices⁵⁴ is shown in Fig. 2. Tensile SiN/AlN films are deposited on the front side of a silicon wafer. Front-side SiN was deposited via low pressure chemical vapor deposition (LPCVD) while AlN was deposited via reactive sputter physical vapor deposition (PVD). SiO₂ is deposited via plasma enhanced chemical vapor deposited (PECVD) on the back side of the wafer to be used as a hard mask for Si Bosch etching. Both front and back sides are patterned by conventional photolithography. SiN and AlN films are patterned and etched first with fluorine- and chlorine-based inductively coupled plasma reactive-ion etching (ICP-RIE), respectively, to define the membrane geometry. The back-side SiO₂ is then patterned and etched with flouorocarbon-based ICP-RIE. The Si wafer is etched from the back-side using patterned SiO₂ as a mask in a deep reactive ion etch (DRIE) Bosch process, leaving approximately

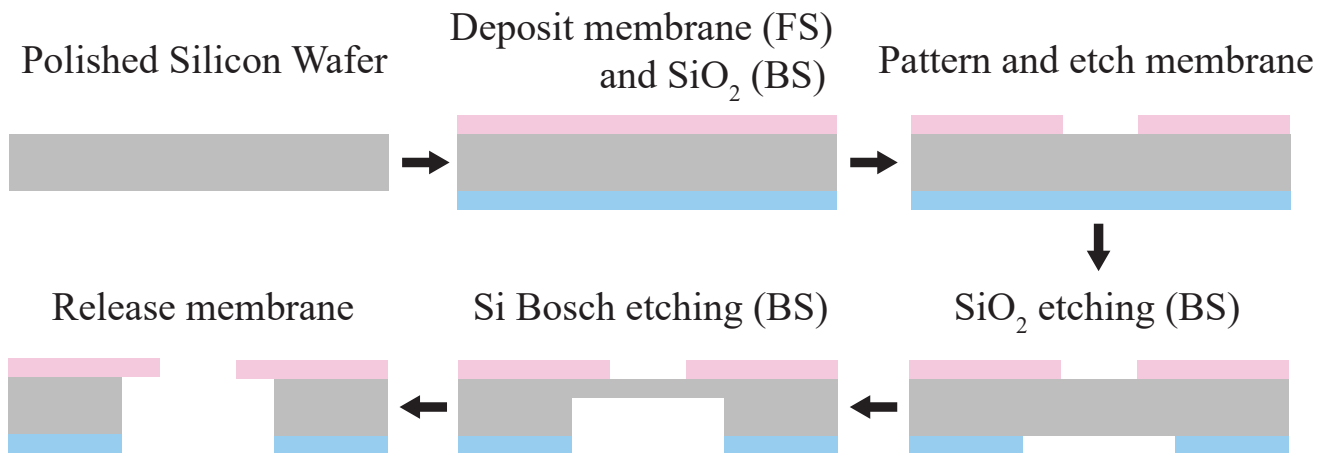


Figure 2. Membrane fabrication process of SiN and AlN; FS is the front side, the top of a silicon wafer, and BS is the back side, the bottom of a silicon wafer. The thickness of membranes is 200 nm, and the membrane transmittance is greater than 95% at 852nm wavelengths (laser cooling light for Cs atoms).

50 μm of Si below the patterned membrane region. Final membrane release is accomplished by a KOH wet etch for SiN membranes, and XeF₂ dry release for AlN membranes. Depending on the shape of membrane holes, an arbitrary shaped MOT can be prepared at the proximity of the membrane MOT devices for interfacing atoms through integrated photonics/electronics.

Trapping atoms in sub-millimeter holes and sub-Doppler cooled atoms

We characterized three different MOT configurations based on location as follows: (1) open space, (2) membrane hole (see Fig. 1 (d): Left), and (3) pierced membrane hole (see Fig. 1 (d): Middle, Right)). Membrane MOT devices can trap atoms in sub-millimeter holes, by measuring steady-state atom number, loading rate, lifetime and sub-Doppler cooled atom temperature compared to the open space MOT atoms. We shared the same laser cooling beams (852 nm, Cs D2 transition) for all the MOT measurements, and the effective MOT beam diameter or the membrane geometry affects those characterization results. Since the atom loading zone is defined by the geometry of membrane holes and the transparent membrane blocks atom trajectory, we regard the membrane hole diameter d_{Hole} as the effective beam diameter d . We found that the membrane MOT ($d \leq 1$ mm, membrane area of 5 mm \times 5 mm) can significantly enhance the number of trapped atoms at the membrane hole due to two large hemi-spherical capture volumes.

We measured the steady-state atom number as shown as Fig. 3. The MOT atom number at the membrane hole decreased by about 5-to-10 times compared to the open space MOT ($d = 3.8$ mm), which may results from lower atom loading rate nearby the membrane device (see Fig. 4 (a)). The pierced membrane MOT devices with a comparable loading rate to the membrane device show even lower atom numbers than that of the membrane MOT devices at the membrane hole due to a lower $1/\beta$ MOT lifetime (see Fig. 4 (b)). The atom number was not much changed depending on a type of membrane (AlN or SiN). The transmittance of membranes should be maximized for a target wavelength, e.g., a laser cooling beam. Using 200nm-thickness AlN and SiN membranes, the transmittance at 852nm wavelengths is greater than 95% and two complete hemispherical capture volumes can be constituted for Cs atoms. The transmittance depends on the thickness and refractive index of the membrane and the light wavelength. In addition, the membrane thickness and the height of the membrane rib can affect the evanescent-field mode of the suspended membrane rib waveguides⁴⁶.

The optical intensity of Gaussian beams is defined as $I(r, z) = P/(\pi w(z)^2/2) \exp(-2r^2/w(z)^2)$, and the beam radius $w(z)$ is the distance from the maximum intensity where the intensity drops to $1/e^2$ ($\approx 13.5\%$). The optical power of each MOT beam is $P = 2.6 \pm 0.2$ mW, and the beam diameter of the MOT beam is $d_{\text{MOT}} = 2w(z) \approx 3.8$ mm at the open space. The intensity of the MOT beam is $I = 17.3 \pm 1.3 I_{\text{sat}}$, where $I_{\text{sat}} = 2.7$ mW/cm² and $\Gamma = 2\pi \cdot 5.2$ MHz (FWHM) for ¹³³Cs D2 transition. We can regard both the MOT beam diameter d_{MOT} and the hole diameter d_{Hole} of membrane MOT devices as the effective beam diameter d for comparison. Using an absorption probe (895 nm, Cs D1 transition), we can measure 6.2×10^5 MOT atoms at the open space ($d_{\text{MOT}} = 3.8$ mm), $1.27 \pm 0.32 \times 10^5$ atoms at the hole of the membrane MOT devices ($d_{\text{Hole}} = 0.4 \sim 1.0$ mm), and 2.1×10^4 atoms at the pierced membrane hole of the membrane device ($d_{\text{Hole}} = 0.4$ mm; a 3- μm -width dummy waveguide), where the detuning of MOT beams is $\delta = 2\Gamma$ and the magnetic field gradient of the MOT coils is $dB/dz \approx 13.6$ G/cm. Regarding the hole diameter d_{Hole} of the membrane MOT devices (photolithography mask pattern) as the effective beam diameter $d = d_{\text{MOT}}$, these results break the $d^{3.6}$ and d^6 scaling laws of MOT atom number for $d_{\text{MOT}} < 1$ mm in a reference⁵³. Starting with 6×10^5 measured atom number at the open space, it is expected to get 0.86 (or 187) atoms ($d_{\text{MOT}} = 0.4$ mm), 10 (or 803) atoms ($d_{\text{MOT}} = 0.6$ mm), and 209 (or 5050) atoms ($d_{\text{MOT}} = 1.0$ mm) based on d^6 scaling (or $d^{3.6}$ scaling). Based on 9.2×10^4 measured atom number at the membrane hole with $d_{\text{Hole}} = 0.4$ mm, we achieve 1.1×10^5 fold increase with d^6 scaling (or 490 fold increase with $d^{3.6}$ scaling). Based on 2.1×10^4 measured atom number at the pierced membrane hole with $d_{\text{Hole}} = 0.4$ mm, we achieve 2.4×10^4 fold increase with d^6 scaling (or 112 fold increase with $d^{3.6}$ scaling). The MOT cloud size is $90 \pm 3 \mu\text{m}$ $1/e^2$ radius.

Based on the loading rate and lifetime measurement of membrane and open space MOTs, we found that the vacuum limited lifetime is the same near and far from the membrane in case of no waveguide, shown in Fig. 5. The loading rate drops by about fourfold near the membrane hole leading to the smaller atom number. A waveguide overlapped with MOT inside the hole significantly decrease the MOT lifetime leading to much smaller atom number.

The usual MOT loading equation⁵⁹ is $N(t) = \frac{\alpha}{\beta}(1 - e^{-\beta t})$, where α is loading rate (atoms/ms) and $1/\beta$ is MOT lifetime (ms); β is loss rate. The steady state atom number of the membrane MOT, α/β , is determined by loading rate and loss rate. Based on reference⁶⁰, the atom number in the MOT is significantly changed depending on the position of MOT atoms from the surface. Additional atom loss increases when the MOT approaches the surface because of atomic collisions with the surface. This attenuates the MOT atom number when the cloud comes less than 300 μm of the surface. For this case, the loading rate (α) is constant (the loading rate probably also decreases when it is getting closer to the surface), whereas the loss rate (β) exhibits a dramatic increase nearby the surface.

The membrane MOT is always centered inside the hole. The distance to the cloud from the membrane hole edge is a half of the hole diameter such as 200, 300, 500 μm for $d_{\text{Hole}} = 0.4, 0.6, 1.0$ mm (photolithography mask pattern). As shown in Fig. 4 (a), loading rates of MOT atoms decrease fourfold near the membrane compared to the open space MOT, which leads

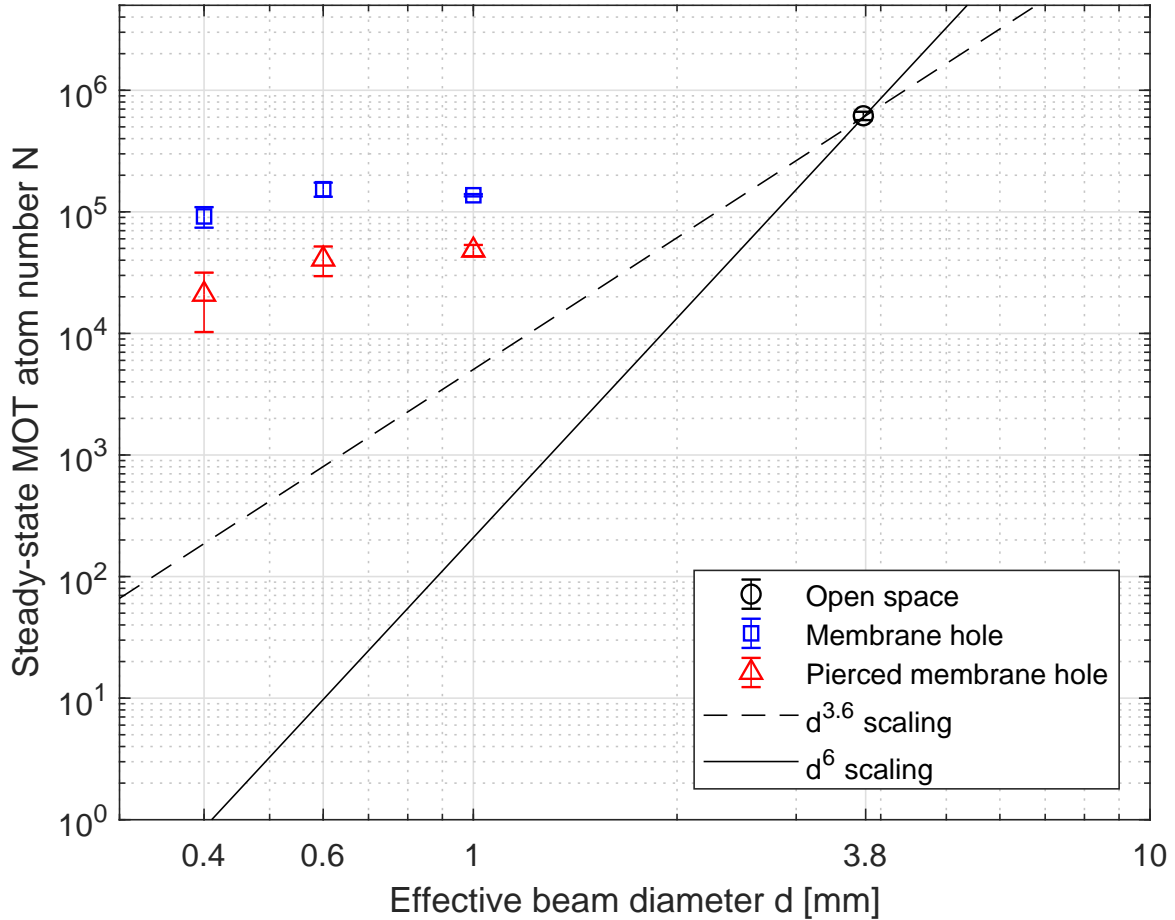


Figure 3. Steady-state MOT atom number N versus effective beam diameter d . The effective beam diameter comes from the Gaussian beam diameter of the MOT beams (d_{MOT} ; $1/e^2$ decrease in intensity) and the hole diameter of the membrane MOT devices (d_{Hole}). The six-beam MOTs were generated by a cooling beam and a repump beam with Cs atoms (852nm, D2 transition). Steady-state MOT atom numbers were measured at the open space (black circle), the membrane hole (blue square), and the pierced membrane hole (red triangle) using an absorption probe (895nm, D1 transition). The $d^{3.6}$ scaling (black dashed line) reaches $N \simeq 190$ at $d = 0.4$ mm and the d^6 scaling comes to $N < 1$ at $d = 0.4$ mm, where the $d^{3.6}$ and the d^6 scalings are extrapolated from the open space MOT data ($N = 6 \times 10^5$). We used a 3.8 mm effective beam diameter ($d = d_{MOT}$) for the open space MOT and 0.4, 0.6, 1.0 mm effective diameters beams ($d \approx d_{Hole}$) for the membrane MOT and the pierced membrane MOT. The pierced membrane MOT experimentally simulates the situation of a 3- μ m-width membrane rib waveguide across the membrane hole.

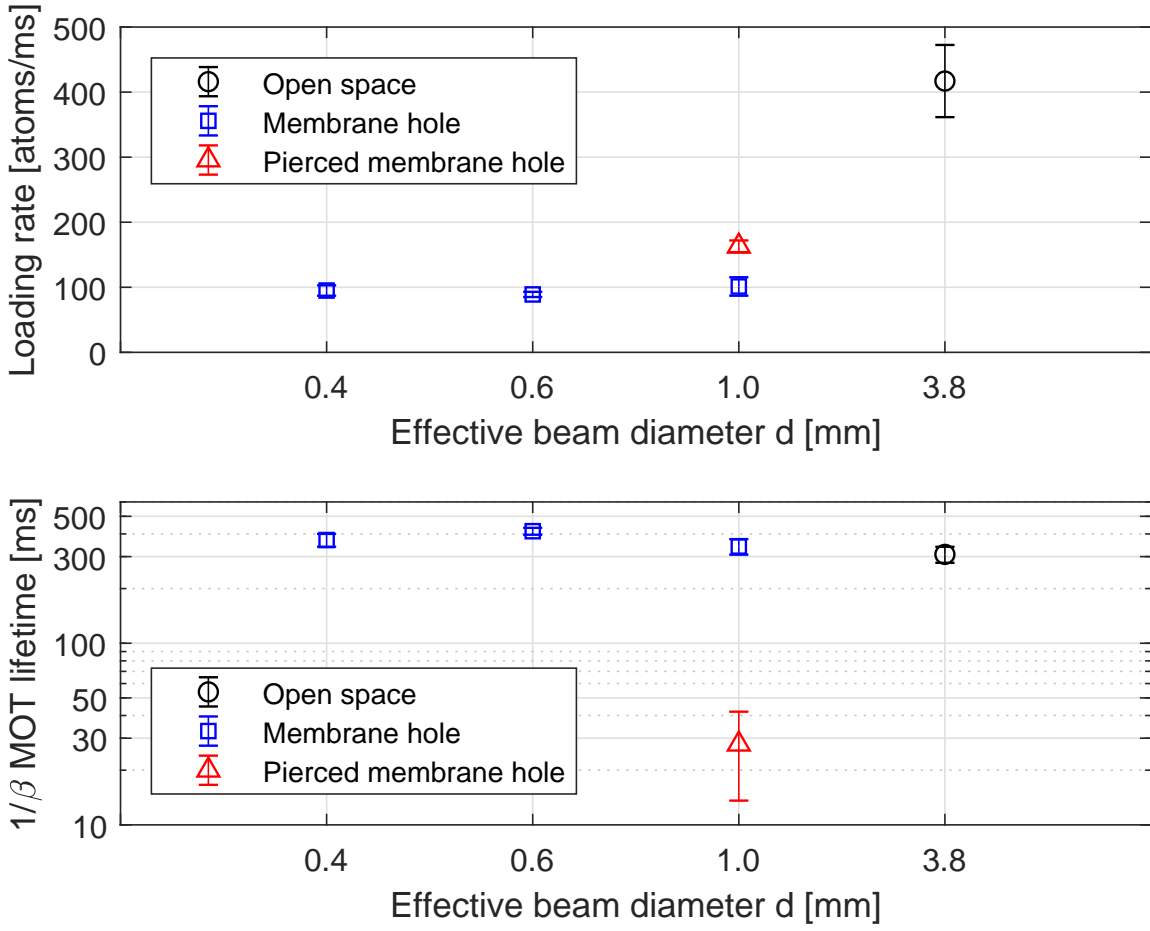


Figure 4. (a) Loading rate versus effective beam diameter d . (b) MOT lifetime versus effective beam diameter d . We measured the loading rates and lifetimes of generated MOT atoms at the open space (black circle), the membrane hole (blue square), and the pierced membrane hole (red triangle). Loading rate and MOT lifetime were measured with an absorption probe. We used 3.8 mm-diameter beams ($d = d_{MOT}$) for the open space MOT (black circle) and 0.4, 0.6, 1.0 mm-diameter beams ($d \approx d_{Hole}$) for the membrane MOT (blue square) and the pierced membrane MOT (red triangle). The pierced membrane MOT experimentally simulates the situation of a 3- μ m-width membrane rib waveguide across the membrane hole.

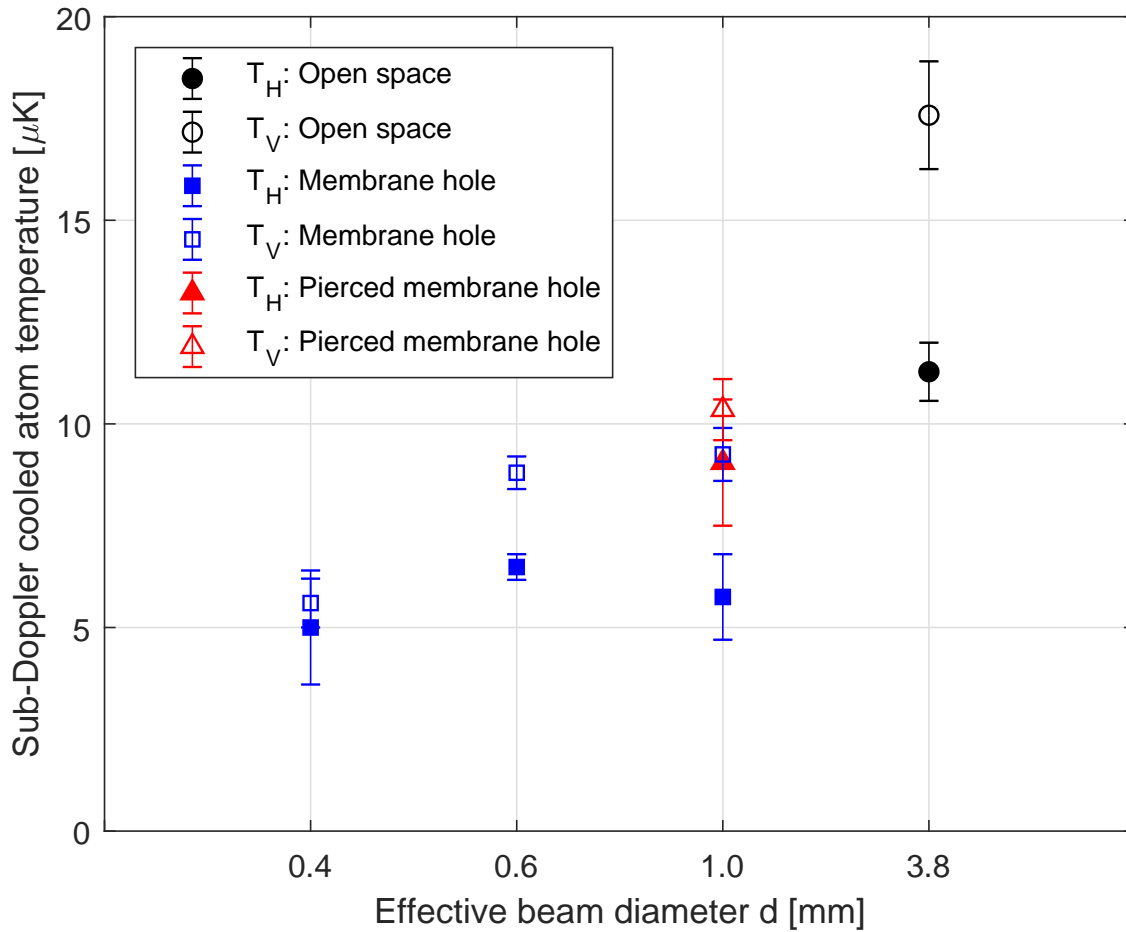


Figure 5. Sub-Doppler cooled temperature of MOT atoms versus effective beam diameter d . For this, we performed a milli-second polarization gradient cooling. We used 3.8 mm-diameter beams ($d = d_{MOT}$) for the open space MOT (black circle) and 0.4, 0.6, 1.0 mm-diameter beams ($d \approx d_{Hole}$) for the membrane MOT (blue square) and the pierced membrane MOT (red triangle). The pierced membrane MOT experimentally simulates the situation of a 3- μ m-width membrane rib waveguide across the membrane hole.

to the smaller steady-state atom number. In addition, the MOT lifetime of the pierced membrane MOT device (red triangle) is significantly lower than other cases, but other membrane MOT devices (blue square) have similar MOT lifetimes of the open space MOT ($d_{MOT} = 3.8$ mm) MOT as shown in Fig. 4 (b). There may exist atomic collisions on waveguide surface resulting in a higher loss rate. Other possibilities include a reduced effective capture volume (partially blocked MOT beams; reduced intensity and impure polarization of cooling beams, surface scattered photons with different k-vectors) and additional waveguide scattered photons with different k-vectors.

We obtained sub-Doppler cooled temperatures of membrane MOT atoms as shown in Fig. 5, which means the membrane MOT will be practical for real-world applications. Starting from steady-state MOTs, polarization gradient (PG) cooling process (1 ~ 2 ms) with intensity lowering and frequency ramping is started while keeping the quadrupole magnetic field on. We measured atom temperature with time-of-flight measurement after sub-Doppler cooling. The temperatures of the open space MOT atoms ($d_{MOT} = 3.8$ mm), membrane MOT atoms ($d_{Hole} = 0.4, 0.6, 1.0$ mm), and pierced membrane MOT atoms ($d_{Hole} = 1.0$ mm) are similar. The pierced section of the membrane MOT devices imitates a 3- μ m-width membrane rib waveguide across the membrane hole. We estimate the temperatures with 2D time-of-flight images. The horizontal temperature (T_H) corresponds to the temperature of atoms on the plane of four horizontal laser cooling beams, and the vertical temperature (T_V) corresponds to the temperature of atoms along the gravity axis of two vertical laser cooling beams as shown in Fig. 1 (b). Both horizontal and vertical temperature follow the trend of the time of flight (TOF) measurements even though the membrane

MOT devices affect the expansion of atoms and there is some uncertainty of estimating the temperature inside the membrane. The temperature of membrane MOTs (blue square) shows a bit lower temperature than the open space MOT (black circle). Probably, hotter atoms during the sub-Doppler cooling process have more chance to hit the membrane and disappear quickly, so we cannot detect those atoms to determine the temperature. The total atom number decreases, but we can achieve colder cloud inside the hole. The lowest cloud temperature of the membrane MOT devices ($d_{Hole} = 0.4\text{ mm}$, blue square) is $5.3\ \mu\text{K}$. The lowest measurable cloud temperature of the pierced membrane MOT devices ($d_{Hole} = 1.0\text{ mm}$, red triangle) is $9.7\ \mu\text{K}$. In the temperature measurement of the sub-Doppler cooled membrane-MOT atoms, the atom number at the membrane hole appears to drop off with drop time as the MOT atoms expand and approach to the membrane. However, the $1/\beta$ MOT lifetime measurement of the Doppler cooled membrane-MOT atoms (Fig. 4(b)) would not limit the atom number for the time scale (1-to-5 ms) of the time-of-flight, temperature, measurement. In particular, the MOT lifetime of the pierced membrane was lower than that of other membranes. We need to study and understand these further for the next step.

Conclusion

We developed membrane MOT devices capable of holding 10^5 cold atoms in a sub-millimeter diameter center hole of the membrane. Sub-Doppler cooling of membrane MOT has been demonstrated as $10\ \mu\text{K}$. Two large hemispherical MOT capture volumes of the membrane MOT devices are generated by six laser-cooled beams through a transparent membrane. This membrane device can accumulate many atoms at the center of the membrane hole during the laser cooling process through the overdamped harmonic motion of an atom, and atoms can dissipate kinetic energy and relax into the center hole without entering the other hemisphere atom loading zone. Based on the effective MOT beam diameter, $400\ \mu\text{m}$ -hole diameter, we measured 10^5 times higher atom number with d^6 scaling. This device was designed to overcome the limited atom-position accessibility onto the membrane rib waveguide by implementing the membrane hole which leads to efficient atom loading around the suspended waveguide across the hole leveraged by two large hemispherical MOT capture volumes. Key enabling technology with the membrane device is to achieve photonic atom trap integrated platforms (ATIP) with neutral atoms having scalability, homogeneous physical properties, long coherence and life times, and room-temperature operability. This membrane MOT devices with integrated photonics can utilize the guided, evanescent-field modes to trap and interface atoms. Integrated photonics/electronics can be additionally fabricated on the membrane device for fulfilling advanced engineering capability required for quantum applications.

Acknowledgement

We thank Peter Schwindt, Matt Eichenfield and Aleem Siddiqui for their support and helpful discussion. This work was supported by the Laboratory Directed Research and Development program at Sandia National Laboratories. Sandia National Laboratories is a multimission laboratory managed and operated by National Technology and Engineering Solutions of Sandia, LLC., a wholly owned subsidiary of Honeywell International, Inc., for the U.S. Department of Energy's National Nuclear Security Administration under contract DE-NA-0003525.

Author contributions statement

Y.-Y. J. was the Principal Investigator and conceived the experiments. J. L. and G. B. conducted the experiments and analyzed the results, and J.L. wrote the manuscript. J.M. and E.D. fabricated membrane MOT devices. All authors reviewed the manuscript.

Additional information

Competing interests The authors declare that they have no competing interests..

References

1. D. S. Weiss, and M. Saffman, "Quantum computing with neutral atoms" *Physics Today* **70**, 7, 44 (2017).
2. C. L. G. Alzar, "Compact chip-scale guided cold atom gyrometers for inertial navigation: Enabling technologies and design study," *AVS Quantum Sci.* 1, 014702 (2019).
3. D. P. DiVincenzo, "The physical implementation of quantum computation, " *Fortschritte der Physik* **48**, 771–783 (2000).
4. L. M. Duan, M. D. Lukin, J. I. Cirac, and P. Zoller, "Long-distance quantum communication with atomic ensembles and linear optics," *Nature* **414**, 413– 418 (2001).

5. X. Qi, Y.-Y. Jau, and I. H. Deutsch, “Enhanced cooperativity for quantum-nondemolition-measurement-induced spin squeezing of atoms coupled to a nanophotonic waveguide,” *Phys. Rev. A* **97**, 033829 (2018).
6. L. Stern, B. Desiatov, I. Goykhman, U. Levy, “Nanoscale light-matter interactions in atomic cladding waveguides,” *Nat. Commun.* **4**, 1548 (2013).
7. J. Lee, D. H. Park, S. Mittal, M. Dagenais and S. L. Rolston, “Integrated optical dipole trap for cold neutral atoms with an optical waveguide coupler,” *New Journal of Physics* **15** 043010 (2013).
8. T. G. Tiecke et al., “Nanophotonic quantum phase switch with a single atom,” *Nature* **508**, 241–244 (2014).
9. A. Goban et al., “Superradiance for atoms trapped along a photonic crystal waveguide”, *Phys. Rev. Lett.* **115**, 063601 (2015).
10. Y. Meng, J. Lee, M. Dagenais, and S. L. Rolston, “A nanowaveguide platform for collective atom-light interaction,” *Appl. Phys. Lett.* **107**, 091110 (2015).
11. T. H. Stievater et al., “Modal characterization of nanophotonic waveguides for atom trapping,” *Opt. Mater. Express* **6**, 3826–3837 (2016).
12. A. T. Black et al., “A Hybrid Nanophotonic-Magnetic Chip-Based Atom Trap,” *Opt. Soc. Am., CLEO: QELS Fundamental Science, FM2H.4* (2018).
13. R. Ritter et al., “Coupling Thermal Atomic Vapor to Slot Waveguides,” *Phys. Rev. X* **8**, 021032 (2018).
14. M. E. Kim, T.-H. Chang, B. M. Fields, C.-A. Chen, C.-L. Hung, “Trapping single atoms on a nanophotonic circuit with configurable tweezer lattices,” *Nature Communications* **10**, 1647 (2019).
15. E. Da Ros, N. Cooper, J. Nute, and L. Hackermueller, “Cold atoms in micromachined waveguides: A new platform for atom-photon interactions,” *Phys. Rev. Res.* **2**, 033098 (2020).
16. J.-B. Béguin et al., “Advanced apparatus for the integration of nanophotonics and cold atoms,” *Optica* Vol. 7, Issue 1, pp. 1-2 (2020).
17. F. Shimizu, K. Shimizu, and H. Takuma, “Four-beam laser trap of neutral atoms,” *Opt. Lett.* **16**, 339–341 (1991).
18. K. I. Lee, J. A. Kim, H. R. Noh, and W. Jhe, “Single-beam atom trap in a pyramidal and conical hollow mirror,” *Opt. Lett.* **21**, 1177–1179 (1996).
19. S. Pollock, J. P. Cotter, A. Laliotis, and E. A. Hinds, “Integrated magneto-optical traps on a chip using silicon pyramid structures,” *Opt. Express* **17**, 14109–14114 (2009).
20. M. Vangeleyn, P. F. Griffin, E. Riis, and A. S. Arnold, “Laser cooling with a single laser beam and a planar diffractor,” *Opt. Lett.* **35**, 3453–3455 (2010).
21. C. C. Nshii et al., “A surface-patterned chip as a strong source of ultracold atoms for quantum technologies,” *Nat. Nanotechnol.* **8**, 321–324 (2013).
22. J. Lee, J. A. Grover, L. A. Orozco, S. L. Rolston, “Sub-Doppler Cooling of Neutral Atoms in a Grating Magneto-Optical Trap,” *J. Opt. Soc. Am. B*, Volume 30, Issue 11, pp. 2869-2874 (2013).
23. A. Hinton et al., “A portable magneto-optical trap with prospects for atom interferometry in civil engineering,” *Phil. Trans. R. Soc. A* **375**: 20160238 (2016).
24. E. Imhof et al., “Two-dimensional grating magneto-optical trap,” *Phys. Rev. A* **96**, 033636 (2017).
25. J. P. McGilligan et al., “Grating chips for quantum technologies,” *Scientific Reports* **7**, Article number: 384 (2017).
26. J. Reichel, W. Hänsel, and T. W. Hänsch, “Atomic micromanipulation with magnetic surface traps,” *Phys. Rev. Lett.* **83**, 3398–3401 (1999).
27. R. Folman et al., “Controlling Cold Atoms using Nanofabricated Surfaces: Atom Chips,” *Phys. Rev. Lett.* **84**, 4749 (2000).
28. K. Brugger et al., “Two-wire guides and traps with vertical bias fields on atom chip,” *Phys. Rev. A* **72**, 023607 (2005).
29. P. D. D. Schwindt, Cornell, E. A., Kishimoto, T., Wang, Y. - J., and Anderson, D. Z., “Efficient loading of a magnetic waveguide on an atom chip”, *Phys. Rev. A* **72** 023612 (2005).
30. Y. Colombe et al., “Strong atom-field coupling for Bose–Einstein condensates in an optical cavity on a chip,” *Nature* **450**, 272–276 (2007).
31. E. A. Salim, S. C. Caliga, J. B. Pfeiffer, and D. Z. Anderson, “High resolution imaging and optical control of Bose-Einstein condensates in an atom chip magnetic trap”, *App. Phys. Lett.* **102**, 084104 (2013).

32. J. A. Rushton, M. Aldous, and M. D. Himsforth, “Contributed Review: The feasibility of a fully miniaturized magneto-optical trap for portable ultracold quantum technology,” *Rev. Sci. Instrum.* **85**, 121501 (2014).
33. M. Keil et al., “Fifteen years of cold matter on the atom chip: promise, realizations, and prospects,” *J. Mod. Opt.* **63**, NO. 18, 1840–1885 (2016).
34. J. Verdú et al., “Strong magnetic coupling of an ultracold gas to a superconducting waveguide cavity,” *Phys. Rev. Lett.* **103**, 043603 (2009).
35. J. E. Hoffman et al., “Atoms talking to SQUIDS,” *Rev. Mex. Fis. S* **57**, 1 (2011).
36. Gershon Kurizki et al., “Quantum technologies with hybrid systems,” *PNAS* **112** (13) 3866-3873 (2015).
37. J. Lee and D. H. Park, ”Protection layers on a superconducting microwave resonator toward a hybrid quantum system,” *Journal of Applied Physics* **115**, 134901 (2015).
38. H. Hattermann et al., “Coupling ultracold atoms to a superconducting coplanar waveguide resonator,” *Nat. Communications* **8**, 2254 (2017).
39. A. W. Elshaari, W. Pernice, K. Srinivasan, O. Benson, and V. Zwiller, “Hybrid integrated quantum photonic circuits,” *Nature Photonics* **14**, 285-298 (2020).
40. A. Kodigala et al., ”Silicon Photonic Single-Sideband Generation with Dual-Parallel Mach-Zehnder Modulators,” *Opt. Soc. Am., CLEO: Science and Innovations, STh4N.6* (2019).
41. A. V. Rakholia, H. J. McGuinness, and G. W. Biedermann, “Dual-Axis High-Data-Rate Atom Interferometer via Cold Ensemble Exchange”, *Phys. Rev. Applied* **2**, 054012 (2014).
42. W. Knight, "IBM Raises the Bar with a 50-Qubit Quantum Computer," *MIT Technology Review*, Dec 13 (2017).
43. F. Arute et al., “Quantum supremacy using a programmable superconducting processor,” *Nature* **574**, 505–510 (2019).
44. J. Zhang et al., "Observation of a many-body dynamical phase transition with a 53-qubit quantum simulator," *Nature* **551**, 601–604 (2017).
45. D. J. Reilly, “Engineering the quantum-classical interface of solid-state qubits,” *npj Quantum Information* **1**, 15011 (2015).
46. Y. B. Ovchinnikov and F. E. Ayi-Yovo, “Towards all-optical atom chips based on optical waveguides,” *New Journal of Physics*, **22**, 053003 (2020).
47. T. Schröder et al., “Quantum nanophotonics in diamond,” *J. Opt. Soc. Am.* **33**, Issue 4, pp. B65-B83 (2016).
48. G. Popkin, “Quest for qubits,” *Science* **354** (6316), 1090-1093 (2016).
49. E. Vetsch et al., “Optical interface created by laser-cooled atoms trapped in the evanescent field surrounding an optical nanofiber,” *Phys. Rev. Lett.* **104**, 203603 (2010).
50. J. Lee, J. A. Grover, J. E. Hoffman, L. A. Orozco, and S. L. Rolston, “Inhomogeneous broadening of optical transitions of 87Rb atoms in an optical nanofiber trap,” *J. Phys. B - At. Mol. Opt.* **48**, 16, 165004 (2015).
51. C. Østfeldt et al., “Dipole force free optical control and cooling of nanofiber trapped atoms,” **42**, 21, pp. 4315-4318 (2017).
52. S. Kato et al., “Observation of dressed states of distant atoms with delocalized photons in coupled-cavities quantum electrodynamics,” *Nature Communications* **10**, 1160 (2019).
53. G. W. Hoth, E. A. Donley, and J. Kitching, “Atom number in magneto-optic traps with millimeter scale laser beams,” *Optics Lett.* **38**, No. 5 (2013).
54. Y.-Y. Jau, and J. Lee, “Microfabricated waveguide atom traps,” United States. Web. doi:10.2172/1396077 (2017). <https://www.osti.gov/servlets/purl/1396077>.
55. J. Dalibard and C. Cohen-Tannoudji, “Laser cooling below the Doppler limit by polarization gradients: simple theoretical models,” *J. Opt. Soc. Am. B* **6**, 2023–2045 (1989).
56. P. J. Ungar, D. S. Weiss, E. Riis, and S. Chu, “Optical molasses and multilevel atoms: theory,” *J. Opt. Soc. Am. B* **6**, 2058–2071 (1989).
57. B. Sheehy, S.-Q. Shang, P. van der Straten, S. Hatamian, and H. Metcalf, “Magnetic-field-induced laser cooling below the Doppler limit,” *Phys. Rev. Lett.* **64**, 858–861 (1990).
58. M. Walhout, J. Dalibard, S. L. Rolston, and W. D. Phillips, “ $\sigma^+ - \sigma^-$ Optical molasses in a longitudinal magnetic field,” *J. Opt. Soc. Am. B* **9**, 1997–2007 (1992).

59. A. M. Steane, M. Chowdhury, and C. J. Foot, "Radiation force in the magneto-optical trap," *Opt. Soc. Am. B* **9**, 2142 (1992).
60. S. Pollock, J. P. Cotter, A. Laliotis, F. Ramirez-Martinez, and E. A. Hinds, "Characteristics of integrated magneto-optical traps for atom chips," *New Journal of Physics* **13** 043029 (2011).

Figures

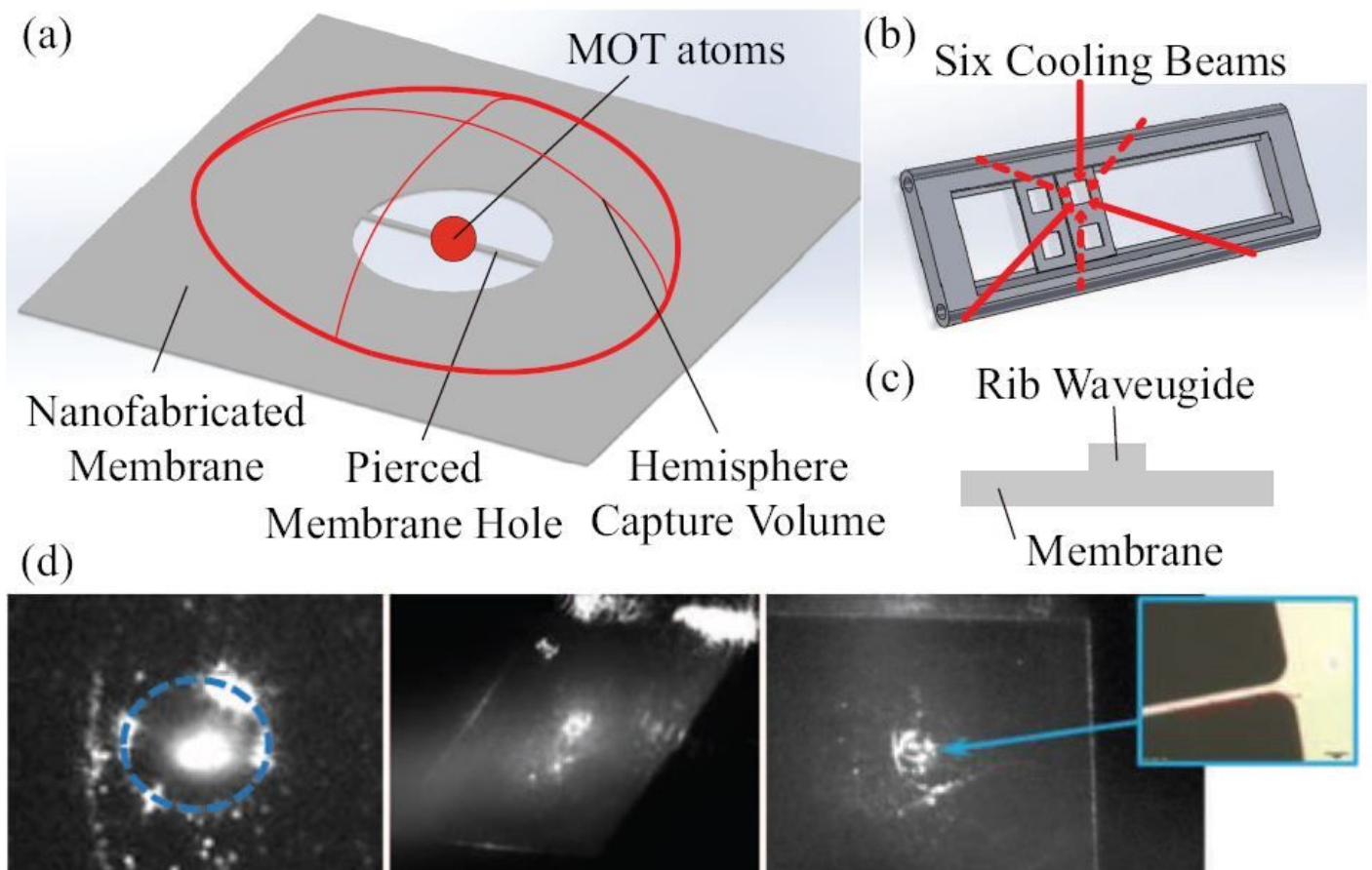


Figure 1

(a) Concept of membrane MOT devices. The area of the membrane is $5 \text{ mm} \times 5 \text{ mm}$, and cold atoms in a membrane MOT can be generated at a sub-millimeter diameter membrane hole using six 3.8 mm -diameter cooling beams. The pierced membrane hole imitates a $3\text{-}\mu\text{m}$ -width membrane rib waveguide, i.e., a dummy waveguide. (b) Six cooling beam configuration. Two membrane MOT devices are fabricated on the silicon substrate ($1 \text{ cm} \times 2 \text{ cm}$), which are attached on the aluminum mount with UV epoxy. (c) Concept of the membrane rib waveguide. (d) (Left) Image of laser-cooled atoms at the center of a membrane hole without a dummy waveguide. The diameter of the membrane hole is $400 \mu\text{m}$. (Middle, Right) Images of laser-cooled atoms at a pierced membrane hole. The diameter of the pierced membrane hole is $400 \mu\text{m}$.

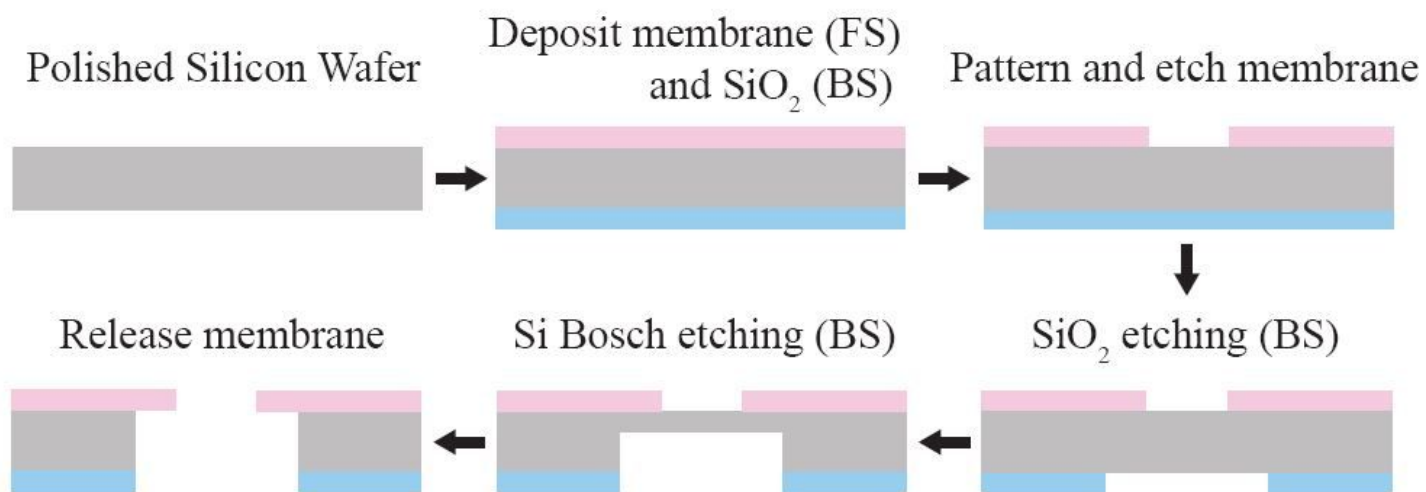


Figure 2

Membrane fabrication process of SiN and AlN; FS is the front side, the top of a silicon wafer, and BS is the back side, the bottom of a silicon wafer. The thickness of membranes is 200 nm, and the membrane transmittance is greater than 95% at 852nm wavelengths (laser cooling light for Cs atoms).

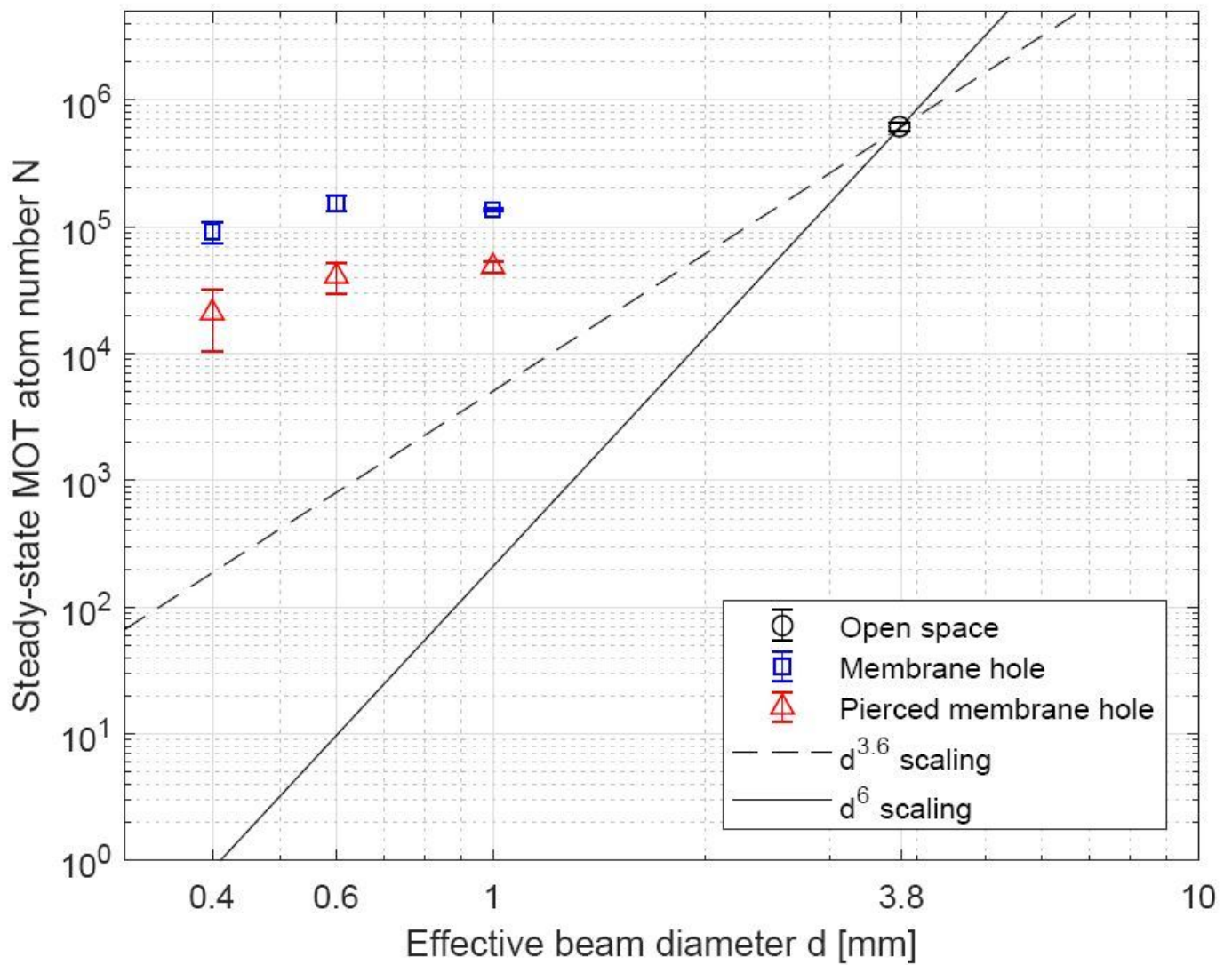


Figure 3

Steady-state MOT atom number N versus effective beam diameter d . The effective beam diameter comes from the Gaussian beam diameter of the MOT beams (d_{MOT} ; $1/e^2$ decrease in intensity) and the hole diameter of the membrane MOT devices (d_{Hole}). The six-beam MOTs were generated by a cooling beam and a repump beam with Cs atoms (852nm, D2 transition). Steady-state MOT atom numbers were measured at the open space (black circle), the membrane hole (blue square), and the pierced membrane hole (red triangle) using an absorption probe (895nm, D1 transition). The $d^{3.6}$ scaling (black dashed line) reaches $N \approx 190$ at $d = 0.4\text{mm}$ and the d^6 scaling comes to $N < 1$ at $d = 0.4\text{mm}$, where the $d^{3.6}$ and the d^6 scalings are extrapolated from the open space MOT data ($N = 6 \times 10^5$). We used a 3.8mm effective beam diameter ($d = d_{\text{MOT}}$) for the open space MOT and 0.4, 0.6, 1.0mm effective diameters beams ($d \approx d_{\text{Hole}}$) for the membrane MOT and the pierced membrane MOT. The pierced membrane MOT experimentally simulates the situation of a 3- μm -width membrane rib waveguide across the membrane hole.

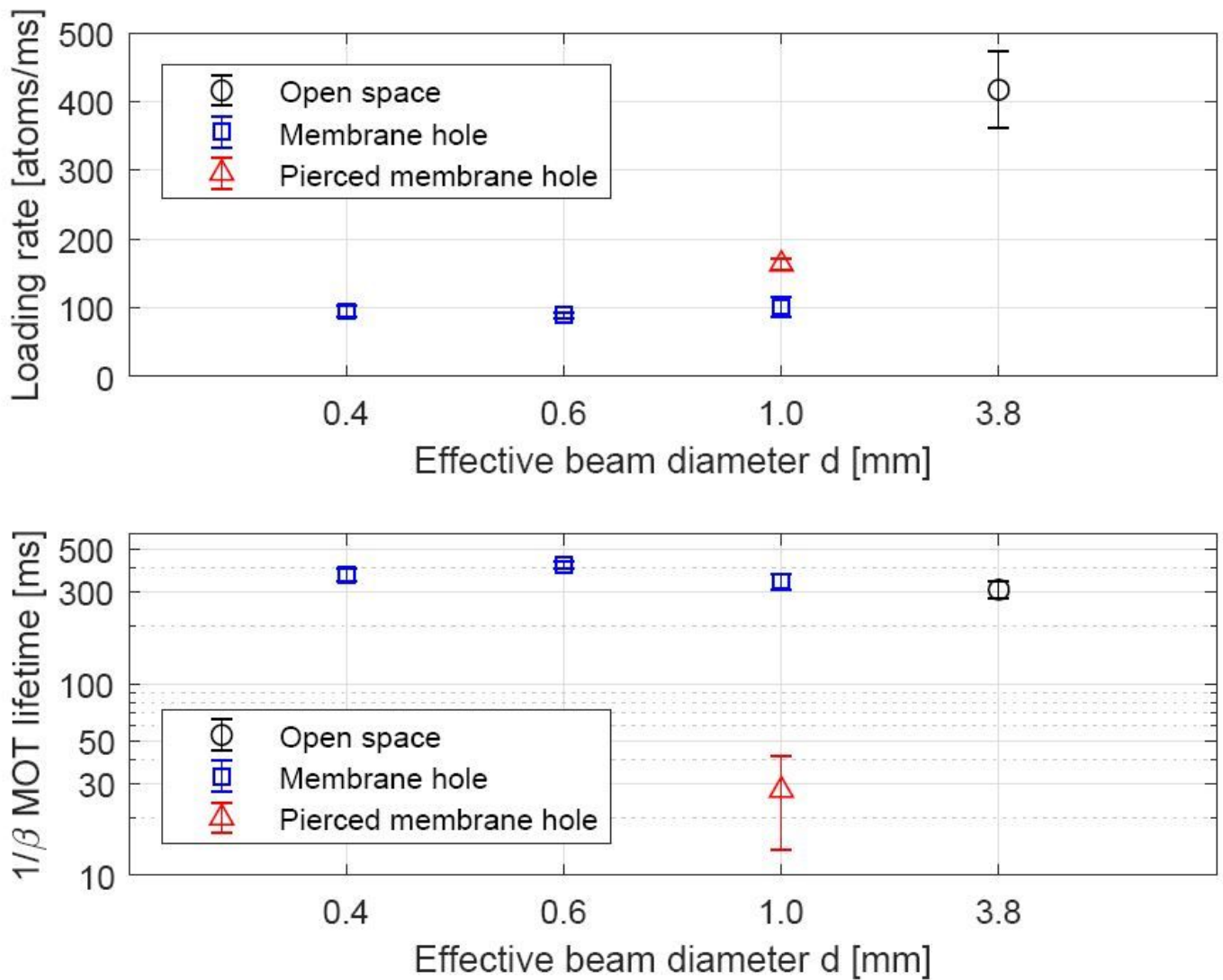


Figure 4

(a) Loading rate versus effective beam diameter d . (b) MOT lifetime versus effective beam diameter d . We measured the loading rates and lifetimes of generated MOT atoms at the open space (black circle), the membrane hole (blue square), and the pierced membrane hole (red triangle). Loading rate and MOT lifetime were measured with an absorption probe. We used 3.8 mm-diameter beams ($d = d_{\text{MOT}}$) for the open space MOT (black circle) and 0.4, 0.6, 1.0 mm-diameter beams ($d \approx d_{\text{Hole}}$) for the membrane MOT (blue square) and the pierced membrane MOT (red triangle). The pierced membrane MOT experimentally simulates the situation of a 3- μm -width membrane rib waveguide across the membrane hole.

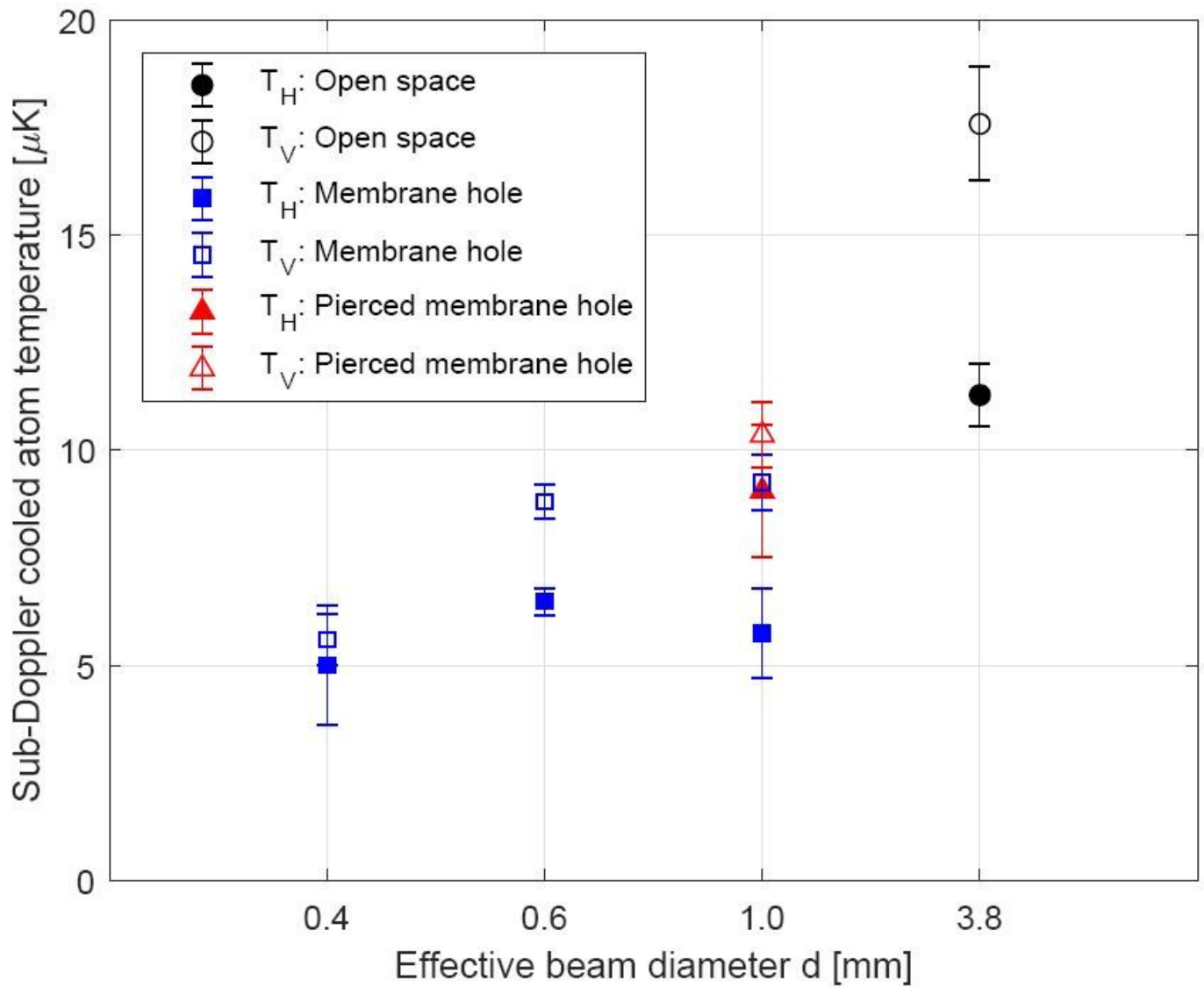


Figure 5

Sub-Doppler cooled temperature of MOT atoms versus effective beam diameter d . For this, we performed a milli-second polarization gradient cooling. We used 3.8 mm-diameter beams ($d = d_{\text{MOT}}$) for the open space MOT (black circle) and 0.4, 0.6, 1.0 mm-diameter beams ($d \approx d_{\text{Hole}}$) for the membrane MOT (blue square) and the pierced membrane MOT (red triangle). The pierced membrane MOT experimentally simulates the situation of a 3- μm -width membrane rib waveguide across the membrane hole.